Lawrence Bernstein, Jonathan Gelbord, Steven Adler-Golden, Nevzat Guler, Robert Sundberg, Spectral Sciences, Inc.; Patrick Conforti, Aerospace Corp. “An improved in-scene atmospheric retrieval and correction algorithm for long-wavelength infrared hyperspectral imagery," Proc. SPIE 10768, Imaging Spectrometry XXII: Applications, Sensors, and Processing (November 2018).

DOI: https://doi.org/10.1117/12.2321116.

See next page for full paper.

Distribution A: Approved for Public Release

An Improved In-Scene Atmospheric Retrieval and Correction Algorithm for Long-Wavelength Infrared Hyperspectral Imagery

Lawrence Bernstein, Jonathan Gelbord[a], Steven Adler-Golden[a], Nevzat Guler[a], Robert Sundberg[*a], and Patrick Conforti[b]

[a]Spectral Sciences, Inc., 4 Fourth Avenue, Burlington, MA, USA 01803

[b]Aerospace Corporation, 14745 Lee Road Chantilly, VA, USA, 20151

ABSTRACT

We describe a new algorithm, QUAC-IR (QUick Atmospheric Correction in the InfraRed), for automated, fast, atmospheric correction of LWIR (Long Wavelength InfraRed) hyperspectral imagery (HSI) and multi-spectral imagery (MSI) in the ~7-14 mm spectral region. QUAC-IR is an in-scene based algorithm, similar to the widely used ISAC (In-Scene Atmospheric Correction) algorithm. It improves upon the ISAC approach in several key ways, including providing absolute, versus relative, sensor-to-ground transmittances and radiances, as well as an estimate of the atmospheric downwelling sky radiance. The latter is important for retrieving emissivity from a reflective (i.e., non-blackbody) pixel. The key aspect of QUAC-IR is that it explicitly searches for blackbody pixels using an efficient approach involving a small number of spectral channels in which the atmospheric radiative transfer is dominated by the water continuum. This allows for fast and simplified Beer's Law (i.e., exponential) scaling of the path transmittance and radiance based on a compact library of pre-computed reference values. We apply QUAC-IR to well-calibrated data from the SEABASS[1] and MAKO[2] HSI sensors. The results are compared to those from a first-principles physics-based atmospheric code, FLAASH-IR.

Key Words: hyperspectral, atmospheric correction, QUAC-IR, sensor, algorithm, LWIR

1. INTRODUCTION

Hyperspectral imaging (HSI) technology provides a wealth of information for remotely identifying and characterizing surface materials and objects based on their spectral signatures. Long-wave infrared (LWIR) HSI data may be analyzed to yield both surface temperatures and emissivity spectra. This requires characterizing and correcting for the atmospheric contributions (transmittance, path radiance and illumination) and retrieving emissivity and temperature from the surface-leaving radiance, a process often referred to as temperature-emissivity separation (TES). Since precise knowledge of atmospheric conditions is rarely available, the atmospheric description is usually derived from the image itself. However, this is not a straightforward task in the LWIR, due to the complexity of the thermal radiation transport phenomenology as well as ambiguity resulting from the fact that the number of unknowns exceeds the number of spectral channels.

A number of algorithms for LWIR HSI atmospheric correction and TES have been developed in recent years. Most rely on first principles atmospheric radiative transfer (RT) calculations[3-9]. An alternative approach developed by Young[10], called the In-Scene Atmospheric Correction (ISAC), relies on locating blackbody or near-blackbody materials in the scene, from which approximate atmospheric transmittance and path (upwelling) radiance are directly extracted. ISAC has a number of drawbacks: the atmospheric spectra are not accurately normalized; there is no information on the illumination (downwelling radiance), which especially impacts the retrieval of low emissivity materials; the blackbody-finding method is not foolproof; and occasionally a scene will not contain blackbodies. Advantages of ISAC include the ability to accommodate some difficult-to-model atmospheric conditions, such as the presence of dust, as well as modest errors in the sensor spectral or radiometric calibration.

*rob@spectral.com; phone 1 781 273-4770 fax 1 781 270-1161; spectral.com

This paper presents a new in-scene method, called QUAC-IR (Quick Atmospheric Correction for the Infrared), for atmospheric retrieval in LWIR HSI. QUAC-IR improves on ISAC in several significant ways. It uses a small set of MODTRAN[11] atmospheric RT calculations that are pre-computed and stored in a spectral library. This allows for efficient removal of non-blackbody pixels and ties the atmospheric spectra to these calculations to produce quantitative transmittance and upwelling radiance spectra. QUAC-IR also provides an estimate of the downwelling radiance. This enables the retrieval of emissivity spectra using a smooth emissivity-based algorithm and improves emissivity accuracy with other methods such as emissivity normalization. Here we describe the QUAC-IR method and show results and comparisons with both ISAC and the FLAASH-IR first principles method[8,9] for example data sets from the well-calibrated SEBASS and MAKO sensors. The advantages of QUAC-IR versus first principles methods include faster computations, code simplicity, the ability to accommodate deviations from ideal conditions, such as a dusty atmosphere and inaccuracy in the sensor spectral and radiometric calibrations, and its applicability to multi-spectral imagery.

2. ATMOSPHERE RETRIEVAL USING BLACKBODIES

The LWIR spectral radiance measured by a sensor viewing objects on the ground (see Figure 1) can be written as

$$L_{obs}(\lambda) = B(T_s, \lambda)\varepsilon(\lambda)\tau(\lambda) + [1 - \varepsilon(\lambda)]L^{\downarrow}(\lambda) + L^{\uparrow}(\lambda) \quad \textbf{(1)}$$

where λ is wavelength, $\varepsilon(\lambda)$ is the composition- and temperature-averaged spectral emissivity of the surface pixel, $\tau(\lambda)$ is the total (diffuse plus direct) transmittance between the surface and the sensor, $B(T_s, \lambda)$ is the surface Planck blackbody function at temperature T_s, $L^{\downarrow}(\lambda)$ is the transmitted incident illumination (it includes the ground-to-sensor transmittance), and $L^{\uparrow}(\lambda)$ is the atmospheric path radiance. T_s is effectively an emissivity-weighted average within each pixel. Eq. (1) is rigorous for Lambertian surfaces; for specular surfaces $\varepsilon(\lambda)$ may be understood as the hemispherical directional emissivity and $L^{\downarrow}(\lambda)$ as an effective quantity involving angular integration over the environment. We assume that the hyperspectral wavelength channels are narrow enough that within-channel variations in emissivity and the Planck function are not of concern. For the common nadir-viewing geometry, the observed surfaces are predominantly horizontal or nearly so, and we assume that they are illuminated only by the atmospheric downwelling radiance. In order to retrieve the pixel-dependent quantities, surface emissivity and temperature, we first need to determine the assumed, image-independent atmospheric quantities, $L^{\uparrow}(\lambda)$, $L^{\downarrow}(\lambda)$, and $\tau(\lambda)$.

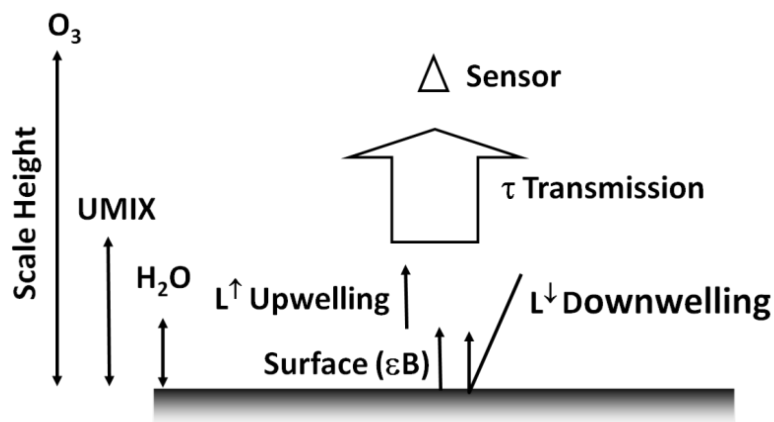

Figure 1. Physics overview of atmospheric effects for LWIR HSI spectral imagery.

Blackbodies, for which $\varepsilon(\lambda)$ is very close to unity, simplify the process of determining some of the atmospheric quantities. Nearly all scenes contain some blackbody or near-blackbody pixels. These pixels may contain vegetation, water, or surfaces subject to strong cavity effects. For such pixels, Eq. (1) becomes dramatically simplified,

$$L_{obs}(\lambda) = B(T_s, \lambda)\tau(\lambda) + L^{\uparrow}(\lambda) \quad \textbf{(2)}$$

If the blackbody pixel temperatures are not all the same and are estimated from an atmospherically transparent wavelength, then a correlation plot of $L_{obs}(\lambda)$ versus $B(T_s, \lambda)$ yields $\tau(\lambda)$ as the slope and $L^{\uparrow}(\lambda)$ as the intercept. $\tau(\lambda)$ can be refined by setting its upper limit to unity, while $L^{\uparrow}(\lambda)$ is independent of any transmittance assumption. $\tau(\lambda)$ can also be refined by rescaling to an RT calculation. As discussed later, $L^{\uparrow}(\lambda)$ and $\tau(\lambda)$ can be combined to provide an estimate of the downwelling atmospheric radiance, $L^{\downarrow}(\lambda)$.

The most challenging part of this analysis is to find reasonably pure blackbody pixels. The method used by ISAC is described in detail elsewhere[10] and briefly summarized here. First, a reference wavelength is found where the pixel brightness temperatures are highest, implying maximum atmospheric transparency; this is typically in the vicinity of 10 microns. Then the pixels are selected for which the reference wavelength yields the highest brightness temperatures; this step weeds out pixels with emissivities well below unity at the reference wavelength. Next, for the remaining pixels a L_{obs} versus $B(T, \lambda)$ correlation plot is constructed at each wavelength, where T is the brightness temperature at the reference wavelength. The top edge of the data cloud defines a smaller set of (presumably) blackbody pixels, from which $\tau(\lambda)$ and $L^{\uparrow}(\lambda)$ are extracted by a regression fit.

The ISAC method of selecting blackbody pixels generally works well, but has a couple of potential failure modes. One is that it assumes that the atmosphere is cooler than the ground, which may not hold in nighttime conditions. Another is that if there are very few blackbodies in the scene, and their temperatures are similar, the top edge of the correlation plot data cloud may be poorly defined, leading to inaccurate $\tau(\lambda)$ and $\tau(\lambda)$results.

3. QUAC-IR METHOD FOR ATMOSPHERE RETRIEVAL

The key steps in of the QUAC-IR algorithm are highlighted in Figure 2. As noted above, QUAC-IR incorporates a novel method for finding blackbody pixels. We first search for candidate blackbody pixels by using a Monte Carlo (i.e., random number) selection approach to uniformly sample locations in the image. We quickly screen each pixel to see if it qualifies as a blackbody pixel. This is done by computing the equivalent blackbody temperatures at a handful of "special" wavelengths spread across the sensor wavelength range and determining whether the standard deviation of the temperatures, $\sigma_{T,}$ is sufficiently small to accept that pixel as a candidate blackbody pixel. Typically, if σ_T<~0.4 K, then we tag the pixel as a candidate blackbody pixel. If this threshold is set too low, then no blackbody pixels are found. On the other hand, if it is set too high then too many poor-quality blackbody pixels are selected. The optimum value of this threshold was found to vary slightly for each sensor over the range of ~0.2-0.6 K. We generally seek ~500 candidate blackbody pixels, which are culled down to the best ~100 blackbody pixels by looking for the best blackbody fits at all the sensor wavelengths.

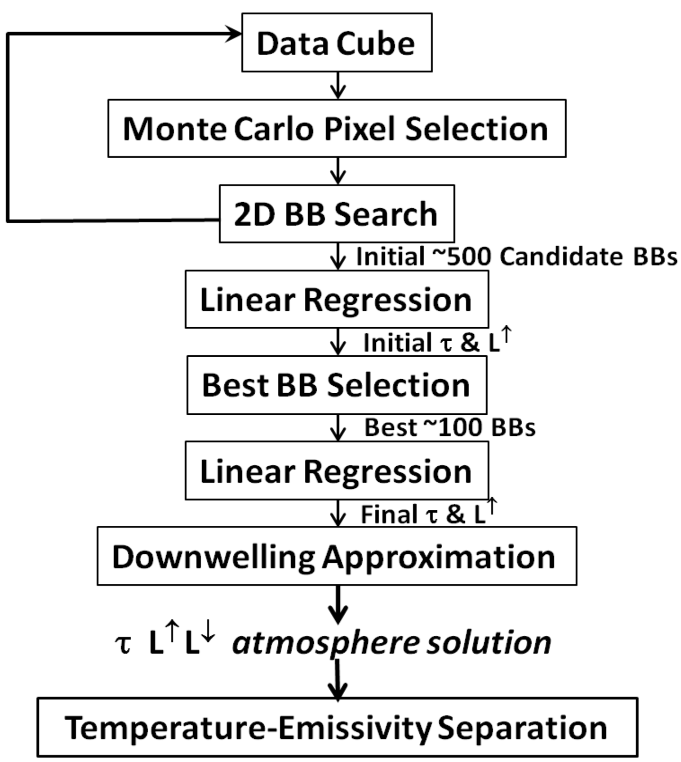

Figure 2. Overview of the key steps of the QUAC-IR algorithm.

The "special" wavelengths used in the initial blackbody screening are indicated in Figure 3. They correspond to spectral regions in which the transmittance is dominated by the water continuum, as opposed to a water line, contribution. The significance of this selection is that for these regions the transmittance approximately obeys Beer's Law. This means that the transmittance for an arbitrary water column amount can be scaled from a reference water column by,

$$\tau(\lambda) = \tau_0(\lambda)^{\alpha}, \tag{3}$$

where τ_0 is the reference transmittance and α is the relative increase or decrease in the water column amount. Because the transmittance doesn't exactly obey Beer's Law (i.e., the power law scaling in eq.(3)), we select a reference transmittance that most closely corresponds to an estimate of the humidity for the image under consideration. The humidity estimate is based on obtaining an estimate of the depth of a strong line feature, such as the 11.7 μm line (see Figure 3.), which depends strongly on humidity. The line depth estimate is obtained from taking the ratio of the standard deviations of the observed image pixels at two nearby wavelengths,

$$\sigma_{Lobs}(\lambda_1)/\ \sigma_{Lobs}(\lambda_2) \approx \tau(\lambda_1)/\ \tau(\lambda_2), \tag{4}$$

where λ_1 is the wavelength at a line transmittance minimum and λ_2 is a nearby transmittance maximum (i.e., 11.6 μm). Given the transmittance ratio, we can distinguish between the three humidity levels in Figure 3 and select the appropriate reference transmittance curve. The same reference transmittance curves can be used for any sensor altitude above the typical water scale height of ~2 km. The physical motivation behind this expression is that (1) the upwelling $L^{\uparrow}(\lambda)$ contribution to $L_{obs}(\lambda)$ (see eq.(1)) is constant across the image (i.e., its variance is zero) and therefore does not contribute to $\sigma_{Lobs}(\lambda)$, and (2) because two nearby wavelengths are used, the ratio of the $B(T_s, \lambda)\varepsilon(\lambda)$ factors at the two wavelengths is close to unity. The largest source of error in this expression arises from the $[1 - \varepsilon(\lambda)]L^{\downarrow}(\lambda)$ downwelling term which adds a wavelength-dependent bias to the standard deviation that is not removed by taking a ratio. However, we minimize the impact of this bias by only including the brightest 50% of the pixels at each wavelength. The brightest pixels tend to have the largest emissivities, ε~1, and therefore minimize the 1-ε~0 reflectance factor in the downwelling term.

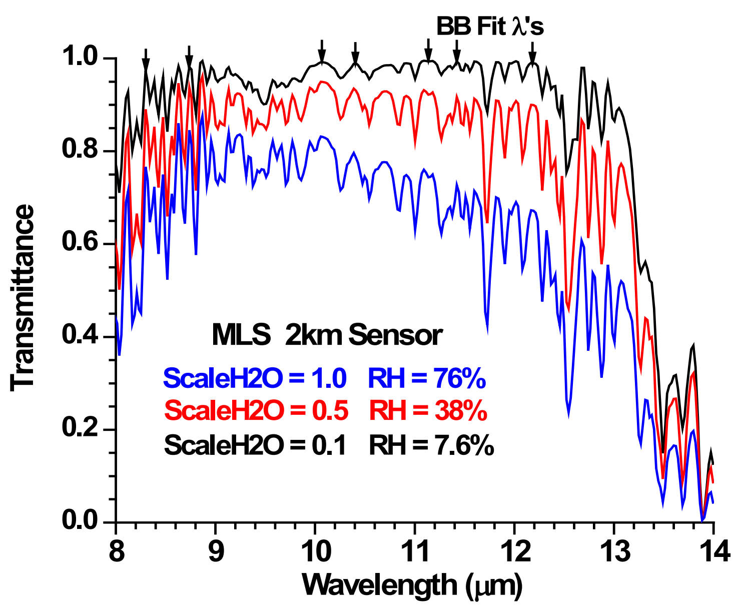

Figure 3. MODTRAN atmospheric transmission calculations for a LWIR HSI sensor showing the relative humidity dependence. The continuum-dominated wavelengths used by QUAC for finding blackbody pixels are indicated by the arrows.

For each candidate blackbody pixel, we perform a 2D Monte Carlo search over potential atmospheric temperatures, T_{atm}, and water column amounts, via the α parameter (see eq.(3), to find the minimum standard deviation of the surface temperatures, σ_T, at the special wavelengths. As mentioned above, if σ_T<~0.4 K, then we tag the pixel as a candidate blackbody pixel. The search is constrained by estimating a plausible range of atmospheric temperatures and water column amounts directly from the data. The search is done by rearranging eq.(2) to estimate the surface blackbody emission at each wavelength using the approximation,

$$B(T_s,\lambda) = (L_{obs}(\lambda) - L^{\uparrow}(\lambda))/\tau(\lambda) \approx = (L_{obs}(\lambda) - (B(T_{atm}, \lambda)\ (1-\tau_0(\lambda)^{\alpha}))/\tau_0(\lambda)^{\alpha}. \quad \textbf{(5)}$$

The temperature at each wavelength is determined by inverting the blackbody function,

$$T_s = (C_2/\lambda)/\ln[C_1/(B(T_s, \lambda)\ \lambda^5)+1], \quad \textbf{(6)}$$

where C_1 and C_2 are the first and second radiation constants, respectively.

An example of the candidate blackbody pixels selected for an airborne data collect over the DOE ARM site at Lamont, OK using the SEBASS sensor is shown in Figure 4. The optimized T_{atm} and water column found separately for each pixel, based on eq.(5), are used to derive the estimated blackbody at all the sensor wavelengths. As seen in Figure 4, this results in relatively smooth, blackbody-like curves. Below ~8 μm and above ~13.5 μm, the atmospheric transmission gets small (see Figure 3), and the corrections become large and unreliable, as is evident from the large fluctuations from blackbody behavior.

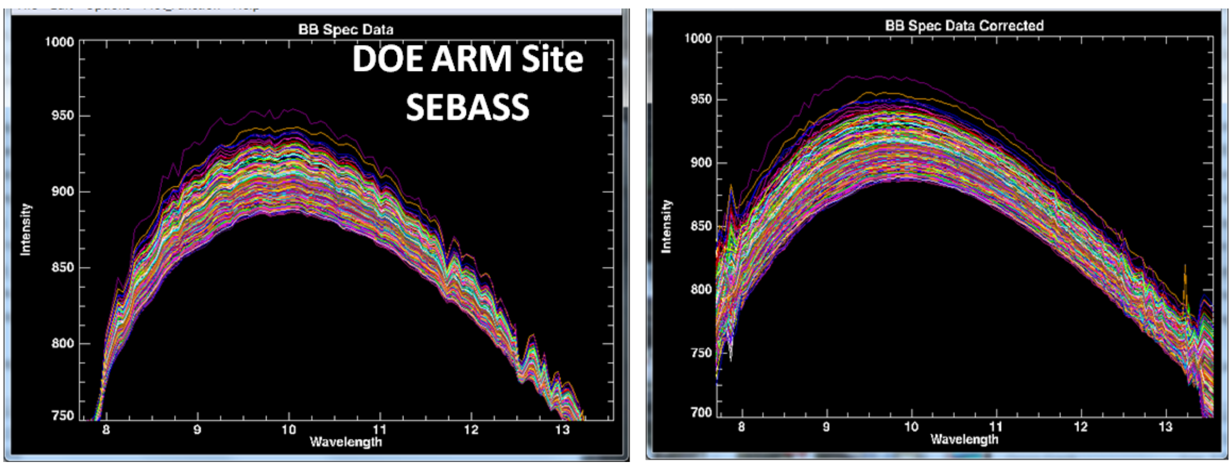

Figure 4. Initial selection of candidate blackbody pixels (left panel) and the resulting effective blackbody functions (right panel) after correction for the path transmittance and upwelling components. Radiance units are microflicks (μF) and wavelength units are microns (μm) throughout this paper.

We use the candidate blackbody pixels to perform an initial linear regression, which provides a good initial estimate of the transmittance, $\tau(\lambda)$, and upwelling, $L^{\uparrow}(\lambda)$, terms. From eq.(3), we see that a plot of $L_{obs}(\lambda)$ versus $B(T_s, \lambda)$ for these pixels will provide $\tau(\lambda)$ from the slope and $L^{\uparrow}(\lambda)$ from the intercept. We require an estimate of the surface temperature, T_s, for each pixel, in order to define $B(T_s, \lambda)$. The temperature estimate is performed using eq.(6) at the sensor channel closest to 10.4 μm, where the atmospheric transmission is at a maximum (see Figure 3) - i.e., the signal is primarily due to the surface blackbody emission. Some example regression plots comparing the blackbody-finding approaches for QUAC-IR and ISAC are shown in Figure 5. The ISAC approach is based on an empirical method for finding potential blackbody pixels. An initial regression is performed and the pixels falling below the linear fit are discarded, as they are deemed to be the least likely blackbody pixels of the initially selected pixels. This procedure may be repeated several times to arrive at a final, best linear fit. The QUAC-IR approach is based on explicitly finding blackbody pixels and, as is evident, provides a tighter linear correlation.

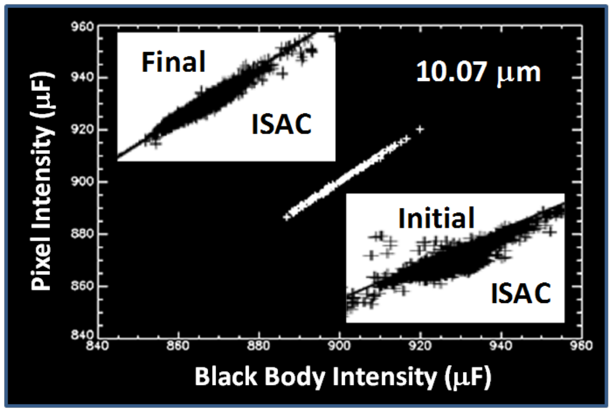

Figure 5. Comparison of the regression curves for QUAC-IR and ISAC for the DOE ARM site SEBASS data.

The initial linear regression provides approximate, relative transmittance and path radiance. We determine the absolute transmittance in two steps. First, the absolute relative humidity (RH) is determined by comparing the ratio of the un-normalized transmittance at two, widely spaced continuum-dominated wavelengths (we use 10.12 μm and 12.18 μm) and comparing to MODTRAN computed ratios. As can be seen in Figure 3, RH is a reasonably sensitive function of this ratio. We note that the ratio is insensitive to the overall normalization factor. Once the RH is found, we normalize the transmittance to a MODTRAN calculation at 10.41 μm, near the transmittance maximum. The correction of the initial relative path radiance requires an additive constant. Determining this constant is equivalent to determining the effective air temperature for the sensor-to-ground path. We can derive the air temperature from the difference in path radiance at two wavelengths, since the unknown constant does not enter into this difference, given by,

$$L^{\uparrow}(\lambda_2)\text{-}\ L^{\uparrow}(\lambda_1) = B(T_{air},\ \lambda_2)[1\text{-}\tau(\lambda_2)]\text{-}\ B(T_{air},\ \lambda_1)[1\text{-}\tau(\lambda_1)]. \quad \textbf{(7)}$$

The only unknown in eq.(7) is T_{air}.

Given the absolute transmittance and path radiance we perform a second linear regression using corrected estimates for T_s (see eq.(2)). The resulting transmittance and path radiance is used to reduce the initial set of candidate blackbody pixels to a final, best set. This is done by using the transmittance and radiance to solve for the effective pixel blackbody curves at all the wavelengths and then culling out those pixels exhibiting the most non-blackbody behavior. We fit the blackbody curves with a fourth order polynomial and look for deviations from the smooth fit. We use a polynomial fit rather than a blackbody fit because it less sensitive to spectral miscalibration. A few examples of the polynomial fit to pixel blackbody curves are shown in Figure 6. As is evident, the candidate blackbody pixels are usually reasonable blackbodies; however small deviations from the smooth fits (and occasionally large deviations) can be seen. Typically, we select the 20% of the pixels that agree the best with their fits.

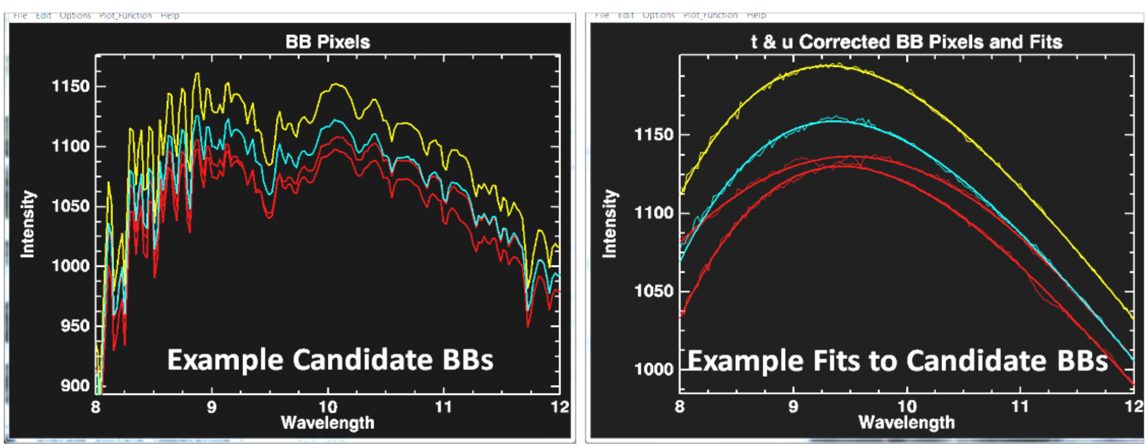

Figure 6. Example candidate blackbody pixels (left plot) and their derived (i.e., via eq.(2) and the regressed transmission and path radiance) and fit curves (right plot). The derived blackbodies are the thinner lines on top of the thicker fits; the small differences between these curves are used to determine the final selection of blackbody pixels.

We use the final selection of blackbody pixels to perform a final linear regression. The resultant transmission and path radiance agrees well with those derived from physics-based approaches, as can be seen in Figure 7. Small differences are noted and it is not always the case that the physics-based approaches produce the best results. They are more susceptible to sensor miscalibration than QUAC-IR.

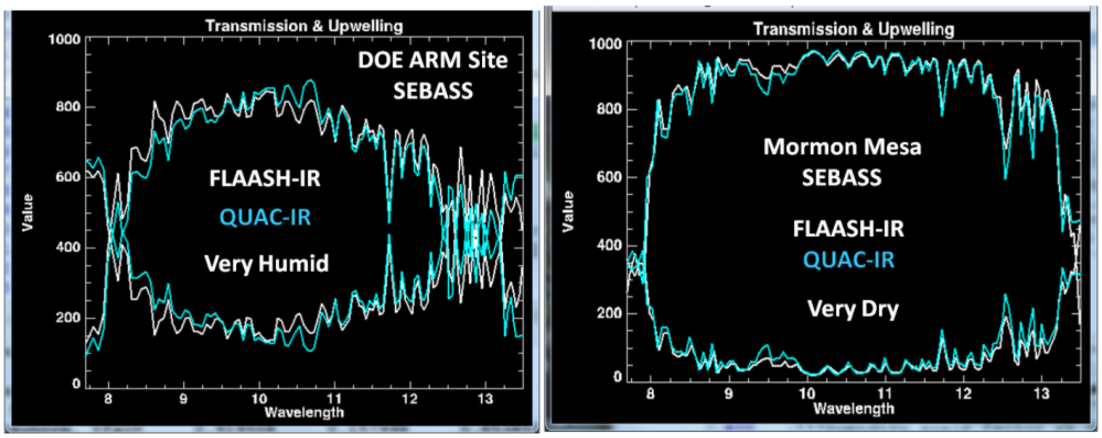

Figure 7. Comparison of QUAC-IR and FLAASH-IR transmittance (x1000) and path radiance (microflicks) for very humid (left plot) and very dry (right plot) atmospheres.

4. EMISSIVITY RETRIEVAL (TEMPERATURE-EMISSIVITY SEPARATION)

FLAASH-IR and QUAC-IR use the same TES algorithm. It is based on re-arrangement of the basic radiance equation, eq.(1), to express the emissivity, $\varepsilon(\lambda)$, in terms of the atmospheric quantities, the transmission and upwelling and downwelling radiances. It yields a family of emissivity spectrum solutions associated with different surface temperatures T_s:

$$\varepsilon(\lambda) = (L_{obs}(\lambda) - L^{\downarrow}(\lambda) - L^{\uparrow}(\lambda)) / (B(T_s,\lambda)\tau(\lambda) - L^{\downarrow}(\lambda)). \quad \textbf{(8)}$$

In order to derive pixel emissivities via a TES algorithm we need to supplement the QUAC-IR transmittance and path radiance with the downwelling contribution. We can derive an approximate downwelling contribution from the transmittance and radiance, based on the assumption that the sensor is above most of the boundary layer humidity. This approach applies to sensors at or above ~2 km altitude. It is also restricted to the spectral range of ~8-13 μm, where water dominates the atmospheric transmission and path emission. Neither of these constraints represents a serious limitation, as most sensors are flown above 2 km, and 8-13 μm spans most, if not all, of the useful data range for most LWIR HSI sensors. The approximate expression for the downwelling is

$$L^{\downarrow}(\lambda) = (1-\tau(\lambda)^{\beta})\tau(\lambda)[L^{\uparrow}(\lambda))/(1-\tau(\lambda))], \quad \textbf{(9)}$$

where β is an empirically determined constant. The term in the square brackets represents the effective source term for the upwelling path emission. In the limit that Beer's Law applied to all the wavelengths and all the surfaces were Lambertian reflectors, then $\beta=2$ would result, because the effective atmospheric emission column amount is about twice that for the upwelling path. We have found that $\beta=0.8$ works the best for most data sets; the large deviation of this value from $\beta=2$ indicates that neither Beer's Law or Lambertian reflection are good approximations for LWIR HSI data.

The QUAC-IR approximation for the downwelling radiance is different from that used in the physics-based codes. The physics-based codes assume Lambertian reflection and require pixels with reflective materials in order to derive the downwelling term based on RT calculations. We compare the QUAC-IR and FLAASH-IR downwelling terms in Figure 8, for SEBASS measurements over the World Trade Center. The most noticeable difference is the missing O_3 contribution for the QUAC-IR downwelling. This arises because most of the O_3 column is above the sensor altitude and hence does not contribute to the path transmission used to estimate the downwelling based on eq. (8). This impacts the QUAC-IR emissivities in the ~9.3-9.8 μm region, where the O_3 emission is significant. It is most noticeable for reflective materials (i.e., ε<~0.7), and the error due to its neglect is proportional to the reflectance - i.e., $R=1-\varepsilon$. However, because the error due to the O_3 contribution has the same spectral shape as the O_3 emission band, it should be relatively straightforward to recognize its presence and remove it via spectral subtraction.

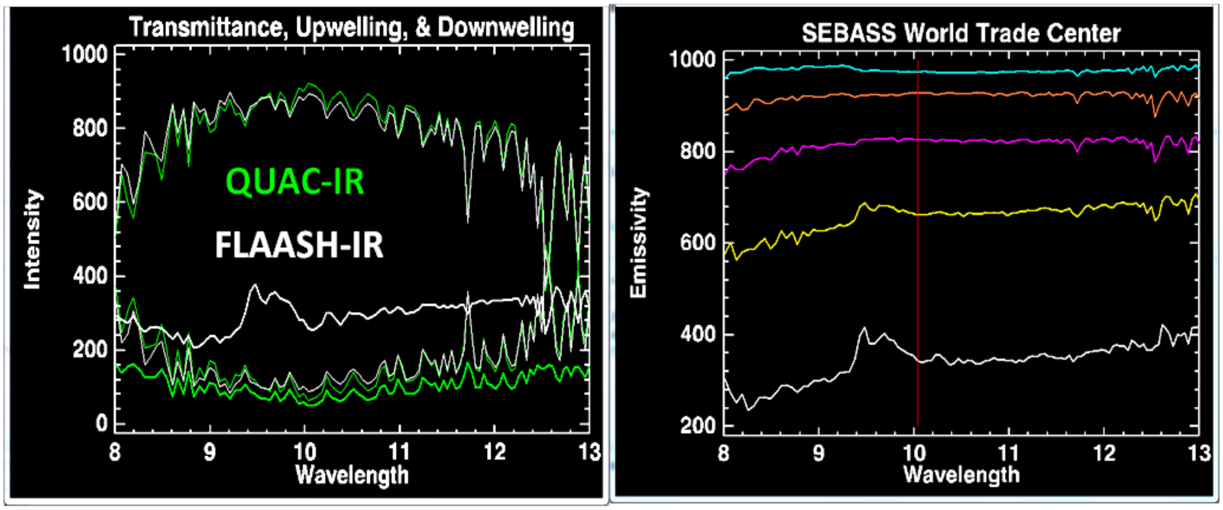

Figure 8. The left plot compares the QUAC-IR and SEBASS transmittance (x1000, top curves), path radiance (bottom curves), and downwelling (intermediate curves). The QUAC-IR downwelling is generally smaller than that for FLAASH-IR and it is missing the O_3 contribution evident in FLAASH-IR. The right plot shows the QUAC-IR retrieved emissivities (x1000) and the impact of the missing O_3 emission downwelling component.

A number of different methods for estimating T_s, and hence ε, have been devised based on plausibility of the ε spectrum. A very simple method is to normalize the maximum of the emissivity spectrum to a typical value, such as 0.98. A second method, which is often used with multispectral data, enforces an empirical relationship between the emissivity spectrum maximum and minimum[12]. These two methods work well for natural terrain but fail for metallic and specular materials, which have higher reflectance. A more sophisticated method for T retrieval uses a library of likely materials, or blends thereof, as trials, finds the combination of material and T that provide the best fit to the pixel spectrum, and then inserts the best-fit T value into Eq. (2) to calculate the emissivity. This method is time consuming but works very well when the library is sufficiently comprehensive.

A versatile and fast method for emissivity retrieval, applicable to nearly all materials, is based on a smooth emissivity assumption[12-15]. Noting that the downwelling radiance, $L^{\downarrow}$, is highly spectrally structured when it is dominated by clear sky, the amount of structure remaining in the ε solution depends on the balance between $L^{\downarrow}$ and $B(T)\tau$ in the denominator of Eq. (2), and thus is a function of T. In the FLAASH-IR[8,9] and Lahaie[14] TES methods, for a given trial T a trial ε is obtained by smoothing the spectrum calculated from Eq. (2), the result is inserted into Eq. (1), the error between the predicted and observed radiance is calculated, and the process is iterated to find the T value that minimizes the error. In FLAASH-IR the smoothing is performed by taking a running average of adjacent spectral points, typically five, whereas Lahaie[13] performs the smoothing with a polynomial fit.

The FLAASH-IR TES method is used with both the QUAC-IR and the FLAASH-IR-derived atmospheric spectra in the example described below. This method cannot be used with ISAC, since ISAC does not provide a downwelling spectrum. While emissivity normalization and the Gillespie method[12] can be used with ISAC, these methods fall apart with reflective surfaces.

5. EXAMPLE RESULTS

5.1 SEBASS data

We illustrate the use of QUAC-IR with an LWIR hyperspectral image acquired in June, 1997 at the US Department of Energy's Atmospheric Radiation Monitoring (ARM) site in Lamont, OK. The image, labeled F8P013, is one of a set acquired with the Aerospace Corp.'s SEBASS sensor[1] from an altitude of 5,000 ft. The scene contains various materials whose spectral emissivities were either known in advance or measured in-situ.

Figure 9 shows a false color emissivity image of the scene with some materials of interest notated. Figure 10 compares the atmospheric spectra retrieved by QUAC-IR, FLAASH-IR, and ISAC. The ISAC implementation is from ENVI (Environment for Visualizing Images, Harris Corp.) with the automated "Max Hits" and "Top of Bins" options. The QUAC-IR and FLAASH-IR transmittance τ and upwelling radiance $L^{\uparrow}$ are in close agreement. The ISAC transmittance spectrum is a relative one; a scale factor of 0.8 would bring it into good agreement with the others, except at a few wavelengths near 10 microns where the retrieval is ill-determined in this implementation. The upwelling radiance can be approximately represented as an emissivity, 1-τ, times an atmospheric Planck function, so a corresponding scaling of the ISAC upwelling spectrum could be made to bring it into reasonable agreement with the others.

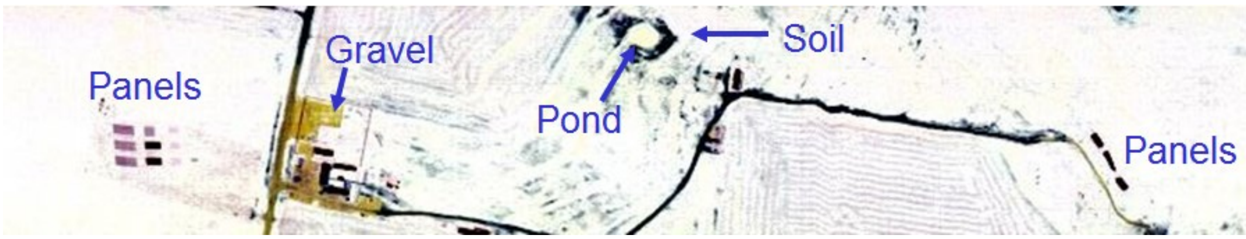

Figure 9. F8P013 emissivity image from FLAASH-IR processing, in false color (R, G, B = 9.25, 10.25, 11.25 microns).

The approximations made in the current QUAC-IR downwelling estimate lead to substantial differences compared with FLAASH-IR, mainly due to underestimated water continuum and missing ozone emission at 9.6 microns. However, the water line structure has roughly the right magnitude, and this is important for retrieving reasonable emissivity spectra for reflective materials.

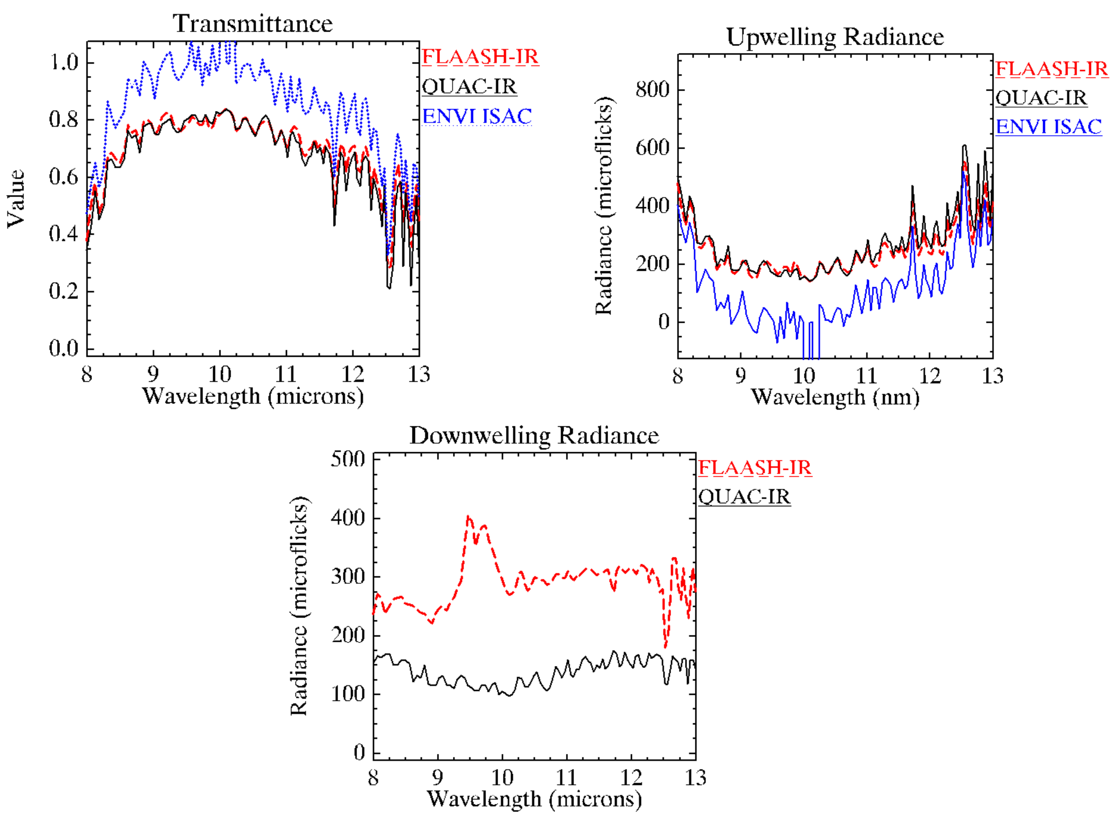

Figure 10. Retrieved atmospheric transmittance, upwelling and downwelling spectra from QUAC-IR, FLAASH-IR and ISAC.

Figure 11 shows several examples of emissivity retrievals from QUAC-IR and FLAASH-IR. For the three higher emissivity materials the results are very similar and agree well with the available "truth" measurements. The QUAC-IR result is especially accurate for the pond pixels, where there is excellent agreement with the true spectrum of water. There is a tendency for FLAASH-IR to generate lower emissivities than QUAC-IR for certain materials or surface temperatures, and in these cases we do not always know which algorithm is more accurate. We have generally found that only with reflective (low emissivity) materials is FLAASH-IR consistently superior to QUAC-IR, due to its more accurate downwelling spectrum. The main difference in shape between the QUAC-IR panel spectrum and the true spectrum is from the 9.6 micron ozone residual.

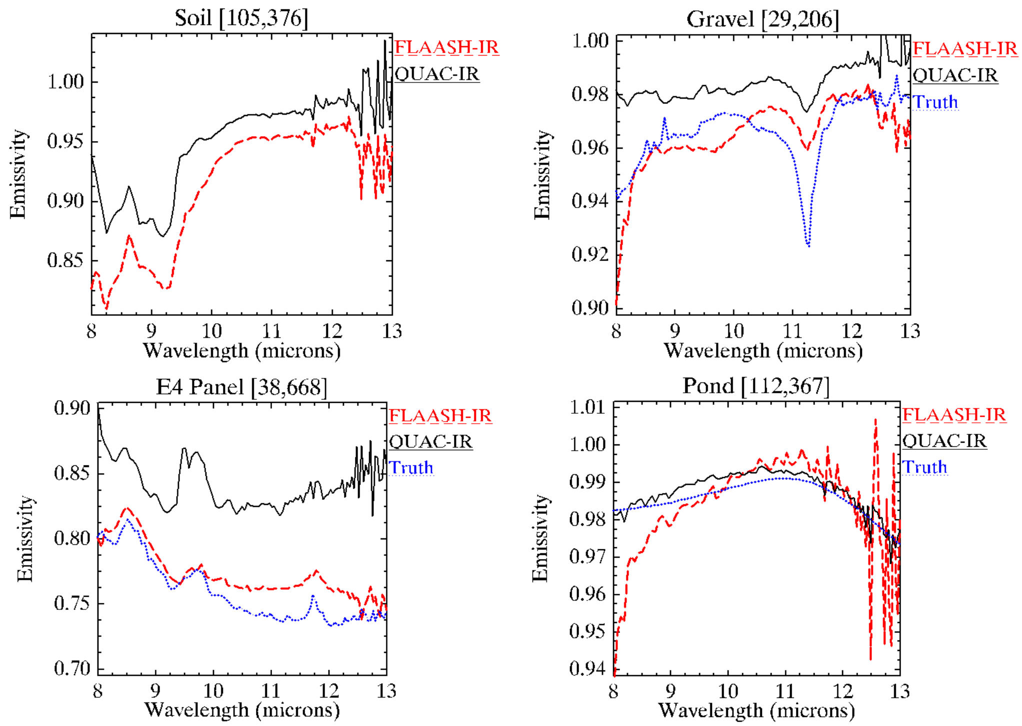

Figure 11. Example emissivity spectrum retrievals.

5.2 MAKO data

As a contrasting example to the agricultural DOE ARM Site, we considered the urban/light industrial scene centered on the Aerospace Corp. facility in El Segundo, CA, as highlighted in Figure 12. This data was collected by the Aerospace Corp. MAKO sensor at an altitude of 6,000 ft. on 22 June, 2017. MAKO is a second-generation follow-on to SEBASS and contains many improvements in the optical and data collection/processing areas[2]. Like SEBASS, MAKO has 128 spectral channels covering the 7.8-13.4 μm spectral region.

The retrieved TUDs (transmittance, upwelling, downwelling) spectra for QUAC-IR and FLAASH-IR are compared in Figure 13. The most notable difference is in the region of the 9.6 μm O_3 band. The O_3 feature is largely absent in the QUAC-IR downwelling spectrum for reasons discussed earlier. While there are small offsets in the transmission and atmospheric path emission spectra, these differences are compensated for by slightly different temperatures in the TES process. Thus, the retrieved emissivities are nearly identical, as can be seen in Figure 14.

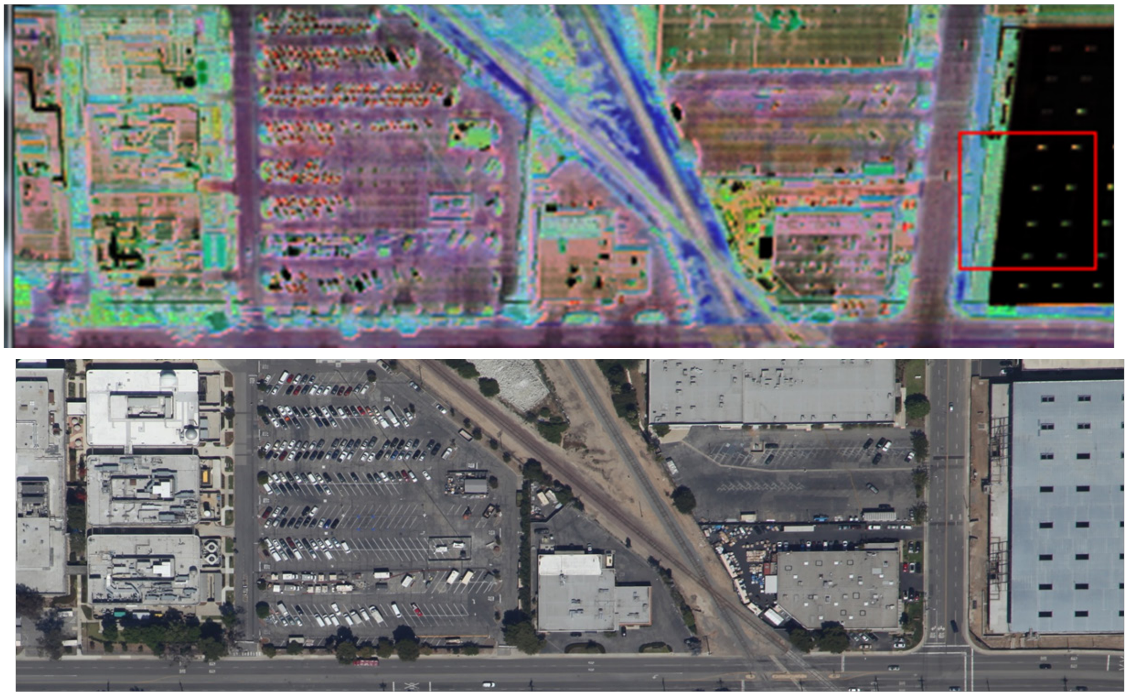

Figure 12. Overview of the area for the MAKO data collection. The top panel is a false color map of the LWIR spectral imagery in which the dark areas correspond to the coldest or most reflective pixels. The bottom panel is a context RGB image of the collection area. The area is centered on the Aerospace Corp. campus.

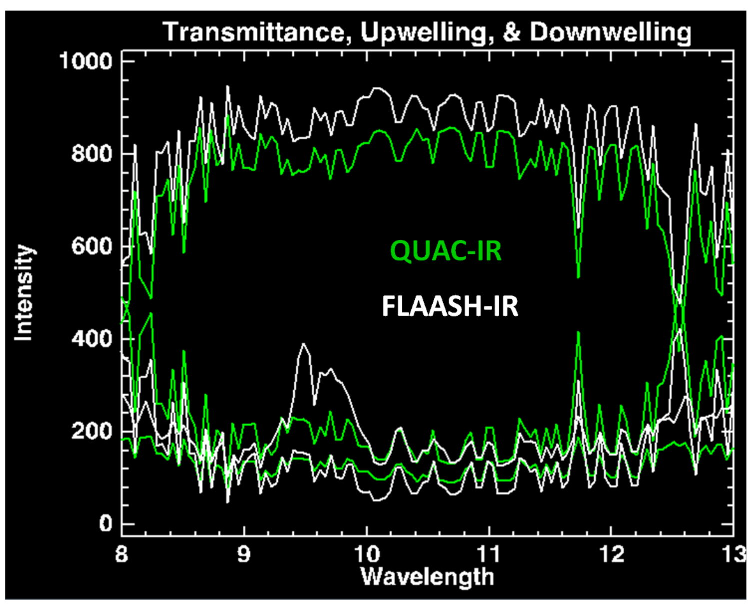

Figure 13. The retrieved TUDs for QUAC-IR and FLAASH-IR.

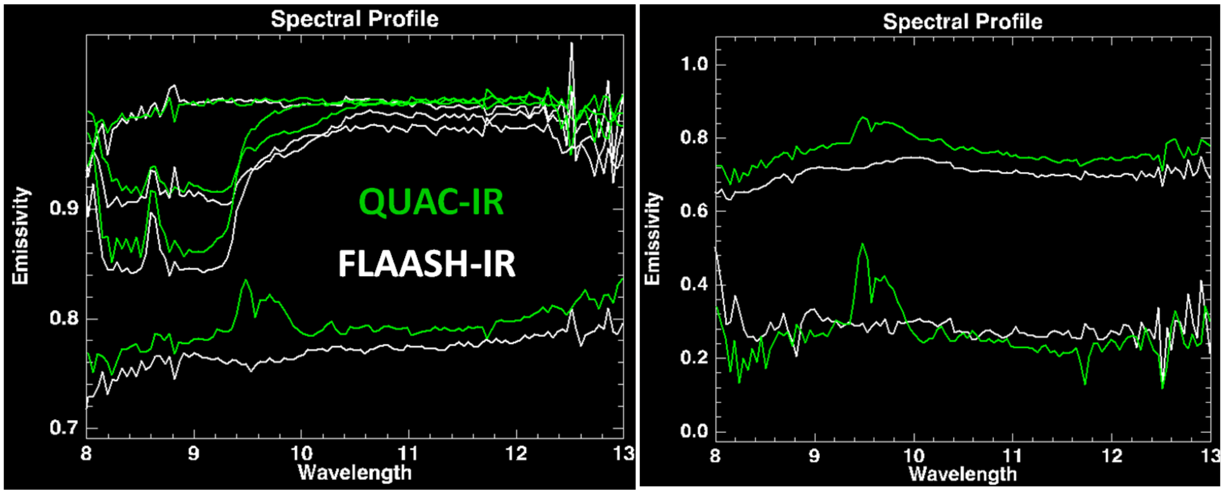

Figure 14. Comparison of retrieved emissivities for QUAC-IR and FLAASH-IR. The left panel compares several emissive pixels, with the highest emissivity corresponding to a tree, the middle spectra to dirt, and the lowest spectrum to a reflective roof. The right panel compares more reflective roof pixels.

6. QUAC-IR SOFTWARE

We have coded QUAC-IR in both IDL/ENVI and C++ languages. The former is useful for efficient implementation and evaluation of new algorithms and the latter is better suited for fast processing in an operational environment. Once a new algorithm has been tested and vetted in IDL/ENVI we then implement it in C++ code. The QUAC-IR source code is relatively compact, comprising ~1000 lines in IDL/ENVI and ~2000 lines in C++. There is a small database, ~15KB, of MODTRAN transmittance calculations. Both versions run quickly on a single CPU. For a SEBASS data cube (128x128 pixels, 128 bands), the IDL/ENVI version took ~0.3 sec to derive TUD spectra and an additional ~2 sec to perform the TES. The C++ version took ~0.1 sec for the TUD and ~0.1 sec for the TES. For comparison, FLAASH-IR took ~1 min to derive the TUD (it used the same TES as for QUAC-IR C++). The time sink for FLAASH-IR, and all other physics-based codes, is the need to run a first principles RT code, MODTRAN in this case.

7. SUMMARY AND CONCLUSIONS

In the example shown here, as well as in many other datasets in which the sensor is located around the top of the atmospheric boundary layer, we have found the new in-scene QUAC-IR method to retrieve quantitative emissivity spectra from LWIR HSI data. Like ISAC, the method is computationally fast and is forgiving of sensor calibration artifacts and difficult-to-model atmospheric conditions. For high emissivity materials, QUAC-IR's accuracy is comparable to that of the first-principles methods, while its ability to generate a downwelling radiance spectrum makes it able to handle much lower emissivities than ISAC. Improvements to the downwelling estimation, particularly with respect to the ozone contribution, can be envisioned, and would lead to further increases in accuracy.

8. ACKNOWLEDGEMENTS

We thank K. Buckland and D. Pratt of the Aerospace Corp. for providing the MAKO data. We thank Spectral Sciences, Inc. for providing IR&D funding to assemble this paper.

REFERENCES

[1] Hackwell, J.A. et al., "LWIR/MWIR Imaging Hyperspectral Sensor for Airborne and Ground-Based Remote Sensing," Proc. of SPIE 2819, Imaging Spectrometry (1996).

[2] Warren, D.W., Boucher, R.H., Gutierrez, D.J., Keim, E.R. and Sivjee, M.G., "MAKO: a high-performance, airborne imaging spectrometer for the long-wave infrared," In Imaging Spectrometry XV Vol. 7812, p. 78120N International Society for Optics and Photonics (2010).

[3] Matsunaga, T., “An Emissivity-Temperature Separation Technique Based on an Empirical Relationship Between Mean and Range of Spectral Emissivity,” Proc. 14th Japanese Conf. of Remote Sensing, pp. 47-48 (1993).
[4] Gu, D., A. R. Gillespie, A. B. Kahle, and F. D. Palluconi, “Autonomous Atmospheric Compensation of High Resolution Hyperspectral Thermal Infrared Remote-Sensing Imagery,” IEEE Trans. Geosci. Remote Sens. 38, pp. 2557-2569 (2000).
[5] Hernandez-Baquero, E.D. and J. R. Schott, “Atmospheric compensation for surface temperature and emissivity separation,” SPIE Proceedings, Algorithms for Multispectral, Hyperspectral, and Ultraspectral Imagery VI, Vol. 4049, pp. 400-410 (2000).
[6] Borel, C.C., “ARTEMISS – an Algorithm to Retrieve Temperature and Emissivity from Hyper-Spectral Thermal Image Data,” 28th Annual GOMACTech Conference, Hyperspectral Imaging Session, Tampa, FL, Los Alamos National Lab. Rpt. No. LA-UR-027907 (2003).
[7] Boonmee, M., J.R. Schott and D.W. Messinger, “Land surface temperature and emissivity retrieval from thermal infrared hyperspectral imagery,” Algorithms and Technologies for Multispectral, Hyperspectral, and Ultraspectral Imagery XII, Sylvia Shen and Paul Lewis, eds., Proc. SPIE 6233, 62331V (2006).
[8] Adler-Golden, S.M., P. Conforti, M. Gagnon, P. Tremblay and M. Chamberland, “Long-wave infrared surface reflectance spectra retrieved from Telops Hyper-Cam imagery,” Proc. SPIE 9088, Algorithms and Technologies for Multispectral, Hyperspectral, and Ultraspectral Imagery XX, 90880U; doi:10.1117/12.2050446 (2014a).
[9] Adler-Golden, S.M., P. Conforti, M. Gagnon, P. Tremblay and M. Chamberland, “Remote sensing of surface emissivity with the Telops Hyper-Cam,” Proc. 6th WHISPERS Conference, Lausanne, 24-27 June (2014b).
[10] Young, S.J., B.R. Johnson and J. A. Hackwell, “An In-scene Method for Atmospheric Compensation of Thermal Hyperspectral Data,” J. Geophys. Res. Atmospheres, Vol. 204, pp. ACH 14-1 – ACH 14-20 (2002).
[11] Berk, A., G.P. Anderson, P.K. Acharya, L.S. Bernstein, L. Muratov, J. Lee, M.J. Fox, S.M. Adler-Golden, J.H. Chetwynd, M.L. Hoke, R.B. Lockwood, T.W. Cooley and J.A. Gardner, “MODTRAN5: a Reformulated Atmospheric Band Model with Auxiliary Species and Practical Multiple Scattering Options,” Proc. SPIE Int. Soc. Opt. Eng. 5655, 88 (2005).
[12] Gillespie, A., S. Rokugawa, S. Hook, T. Matsunaga, and A.B. Kahle, “Temperature/Emissivity Separation Algorithm Theoretical Basis Document, Version 2.4,” NASA Contract NAS531372, March (1999).
[13] Borel, C.C., “Iterative Retrieval of Surface Emissivity and Temperature for a Hyperspectral Sensor,” First JPL Workshop on Remote Sensing of Land Surface Emissivity, May 6-8, pp. 1-5 (1997).
[14] Lahaie, P., “A Temperature and Emissivity Separation Technique for Thermal Hyperspectral Imagers,” ADA469520, available from NTIS and http://www.dtic.mil/cgi-bin/GetTRDoc?AD=ADA469520&Location=U2&doc=GetTRDoc.pdf (2005).
[15] Wang, X., X.Y. Ouyang, B.H. Tang, Z.-L. Li, and R.H. Zhang, “A New Method for Temperature/Emissivity Separation from Hyperspectral Thermal Infrared Data,” Proc. IEEE International Geoscience and Remote Sensing Symposium, Boston, MA, III, pp. 286–9 (2008).